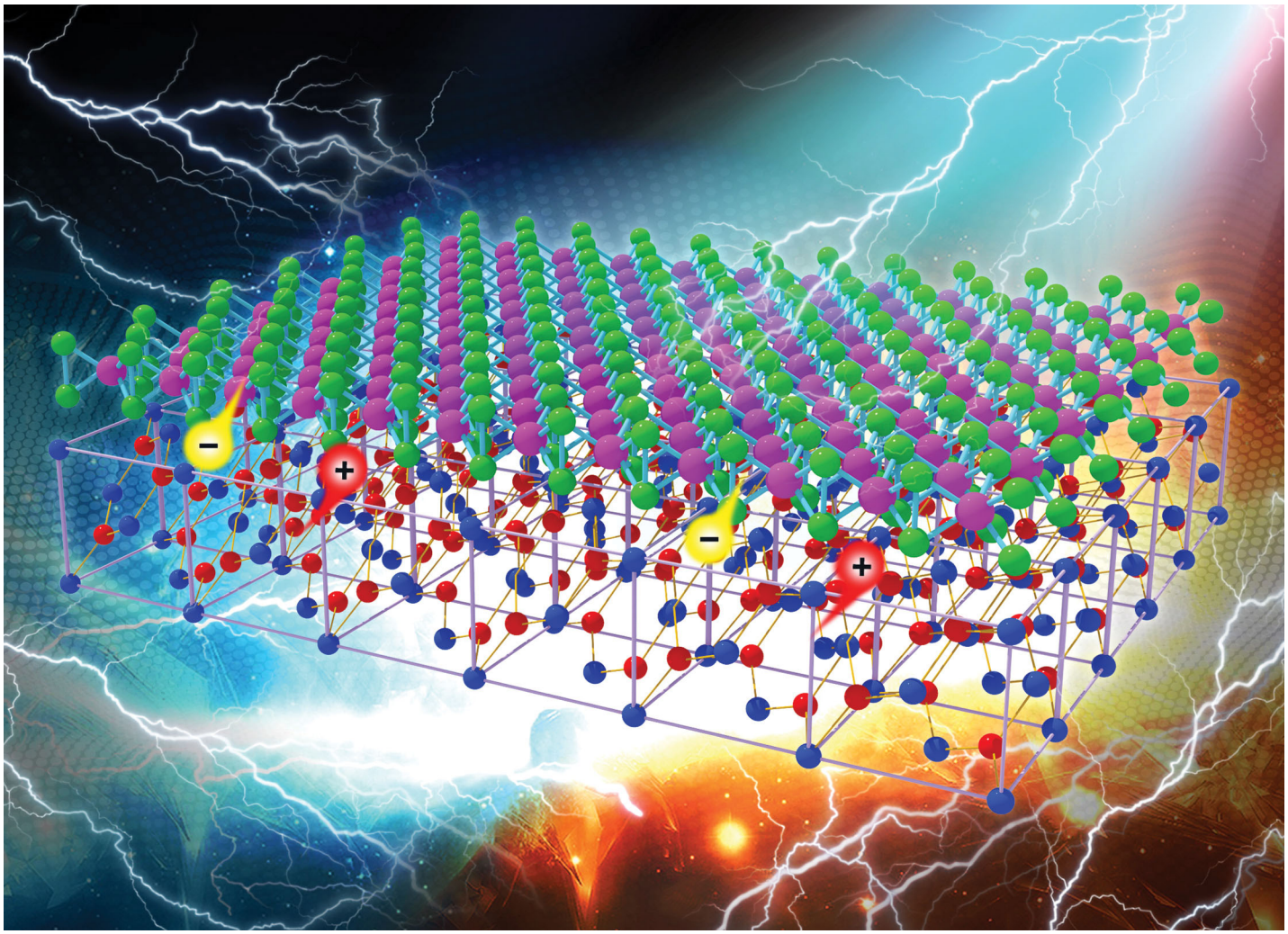

Showcasing collaborative research from University of Electronic Science and Technology of China, China, Fudan University, China and Nanyang Technological University, Singapore.

A 3D topological Dirac semimetal/MoO_3 thin film heterojunction infrared photodetector with a current reversal phenomenon

A 3D DSM $(Cd_{1-x}Zn_x)_3As_2/MoO_3$ heterojunction with current reversal phenomenon is reported, providing a suitable method for preparing high-performance photodetectors in the field of infrared telecommunications and imaging.

As featured in:

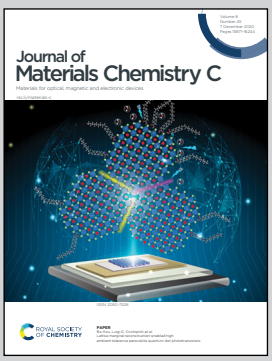

See Faxian Xiu, Jun Wang *et al.*, *J. Mater. Chem. C*, 2020, **8**, 16024.

ROYAL SOCIETY OF CHEMISTRY

rsc.li/materials-c

Registered charity number: 207890

Journal of Materials Chemistry C

ROYAL SOCIETY OF CHEMISTRY

PAPER

View Article Online
View Journal | View Issue

Cite this: J. Mater. Chem. C, 2020, 8, 16024

A 3D topological Dirac semimetal/MoO_3 thin film heterojunction infrared photodetector with a current reversal phenomenon†

Ming Yang,[a] Yunkun Yang,[b] Qi Liu,[a] Hongxi Zhou,[a] Jiayue Han,[a] Xiaoyi Xie,[b] Faxian Xiu,*[b] Jun Gou,[ac] Zhiming Wu,[ac] Zehua Hu,[d] Ting Yu,[d] Jun Wang *[ac] and Yadong Jiang[ac]

Received 17th July 2020,
Accepted 14th August 2020

DOI: 10.1039/d0tc03374j

rsc.li/materials-c

Photoelectric detection technology is extremely significant on account of its extensive applications in commercial and military fields, but high-performance array photodetectors based on Dirac semimetal thin film materials are rarely reported. Hence, we demonstrate photodetectors based on a three dimensional (3D) topological Dirac semimetal (DSM) $(Cd_{1-x}Zn_x)_3As_2/MoO_3$ array heterojunction, showing ultrahigh photoresponsivity, detectivity and external quantum efficiency in the ultra-broadband spectrum (405–4500 nm) of 3.1 A W^{-1}, 6.4 × 10^{10} Jones and 855.8%, respectively, meanwhile possessing array unit performance repeatability and excellent time stability under atmospheric conditions at room temperature. The device exhibits an incredible current reversal phenomenon under the action of both light illumination and temperature variation elements, which can be attributed to a thermoelectromotive force effect. These excellent photoelectric properties illustrate that the fabrication of the 3D DSMs/inorganic thin film heterojunction is a suitable method for preparing distinguished infrared array photodetectors in the field of infrared telecommunications and scanning imaging.

1. Introduction

Photodetectors, converting light signals into electrical current, have demonstrated a wide range of applications in the military and civilian fields, including remote sensing, telecommunications, motion detection, video imaging and so on.[1–3] Traditional 3D thin film photodetectors, *e.g.* InGaAs photodetectors, with their exquisite integrated technology and large-scale production, have been dominating the commercial photodetector market for many years.[4,5] However, the wavelengths of these detectors only covers from visible light (VL) to the near-infrared (NIR) region, leaving the mid-IR region unreached. Over the past decade, two-dimensional (2D) layered materials have rapidly become the most promising components of state-of-the-art detectors due to their unique crystal structure and material diversity.[6–8] In addition-, graphene-, black phosphorus (BP)- and 2D transition metal dichalcogenide (TMD) material-based photodetectors have been highly researched due to their superior gate adjustability and photoresponsivity.[5,6,9–11] Nevertheless, the photoelectric detection application of zero band-gap graphene is restricted by its only 2.3% (monolayer) light absorption and high dark current (I_{dark})[12,13] and BP and TMDs are limited by their poor stability and low response in the infrared (IR) region, respectively,[14–18] and furthermore, there are difficulties for large scale fabrication.[4,10,17–19] Therefore, it is very urgent that we search for new semiconductor materials with outstanding photoelectric characters (for example, stable physico-chemical properties and high absorption) in the IR region.

In recent years, electron transport in the Dirac systems has expanded to 3D systems after the discovery of topological Dirac semimetals (DSMs) in experiments.[19–24] The unique Dirac dispersion is formed by the contact between finite pairs of Dirac conduction bands and valence bands in the 3D systems.[12–14,20–22] Among DSMs, Cd_3As_2 is a potential candidate due to its high optical absorption ratio in the IR region, superior charge carrier mobility and fast response.[15–18] However, since pure Cd_3As_2 possesses a Dirac topological surface state (TSS), it leads to large I_{dark} of Cd_3As_2-based photoelectric devices and limits the intrinsic responsivity of Cd_3As_2-based devices.[19,20,23,24] To reduce the electron density and open the band-gap, Zn doping is used to compensate

[a] School of Optoelectronic Science and Engineering, University of Electronic Science and Technology of China, Chengdu 610054, P. R. China
[b] State Key Laboratory of Surface Physics and Department of Physics, Fudan University, Shanghai 200433, P. R. China. E-mail: faxian@fudan.edu.cn
[c] State Key Laboratory of Electronic Thin Films and Integrated Devices, University of Electronic Science and Technology of China, Chengdu 610054, P. R. China. E-mail: wjun@uestc.edu.cn
[d] Division of Physics and Applied Physics, School of Physical and Mathematical Sciences, Nanyang Technological University, Singapore 637371, Singapore

† Electronic supplementary information (ESI) available: A preparation flow chart of the $(Cd_{1-x}Zn_x)_3As_2/MoO_3$ thin film heterojunction array device, XPS pattern of $(Cd_{1-x}Zn_x)_3As_2$ thin film and the I_{ph} curves of the device under different laser power densities and so on. See DOI: 10.1039/d0tc03374j

the residual electron concentration of Cd_3As_2, forming a novel type of 3D DSMs $(Cd_{1-x}Zn_x)_3As_2$ with a moderate band-gap of ~50 to 100 meV.[24–27] However, after Zn doping, the carrier concentration and mobility will be reduced. To overcome this problem, the best solution is to take appropriate materials to prepare a heterojunction with $(Cd_{1-x}Zn_x)_3As_2$.[28,29]

In this article, we present 3D DSM $(Cd_{1-x}Zn_x)_3As_2/MoO_3$ thin film heterojunction array photodetectors with a broadband detection capability to address the aforementioned key technological requirements. The 2.7 eV band-gap (large enough to suppress I_{dark}), with low-cost, environmentally friendly and easy to achieve large scale preparation of MoO_3 suited to integrate with DSMs to manufacture inorganic thin film heterojunction photodetectors.[29–32] Hence, the device design has the advantage of both the chemical doping and P–N heterostructure scheme, achieving high photoresponsivity (R_i), external quantum efficiency (EQE) and detectivity (D^*) from VL to the low attenuation mid-IR region (4500 nm). In particular, the device possesses characteristics of current reversal, providing an implemented way for application of DSMs.

2. Results and discussion

According to growth characteristics of the $(Cd_{1-x}Zn_x)_3As_2$ thin film, the device adopts a planar heterojunction structure.[33,34] We demonstrate the manufacturing process of the $(Cd_{1-x}Zn_x)_3As_2/MoO_3$ thin film heterojunction array photodetector (Fig. S1, ESI†). $(Cd_{1-x}Zn_x)_3As_2$ and MoO_3 thin films are prepared by the molecular beam epitaxy (MBE) and thermal evaporation system in sequence on sapphire substrates, then post-treated by annealing.[35,36] Fig. 1a and b display the schematic diagrams of $(Cd_{1-x}Zn_x)_3As_2/MoO_3$ thin film heterojunction array device and atomic force microscope (AFM) diagram of the junction area, with a height of ~100 nm. The sudden uplift in Fig. 1b belongs to the sticking needle phenomenon caused by the AFM probe and elements in the thin film during testing. Fig. 1c and d demonstrate surface topography of $(Cd_{1-x}Zn_x)_3As_2$ and MoO_3 thin films. The root-mean-square (RMS) roughness of $(Cd_{1-x}Zn_x)_3As_2$ and MoO_3 are 22.6 nm and 4.8 nm, respectively. In addition, the X-ray photoelectron spectroscopy (XPS) pattern of the 100 nm $(Cd_{1-x}Zn_x)_3As_2$ thin film shown in Fig. S2 (ESI†), demonstrates that the Zn element has been completely doped during the growth process. The energy disperse spectroscopy (EDS) mapping of the $(Cd_{1-x}Zn_x)_3As_2$ thin film demonstrates that Zn has been uniformly doped (Fig. S3, ESI†). Meanwhile, the charge transport properties (mobility, carrier type, conductivity and so on) of the prepared $(Cd_{1-x}Zn_x)_3As_2$ thin film is tested by the Vanderbilt methodd (Table S1, ESI†), showing that the prepared $(Cd_{1-x}Zn_x)_3As_2$ thin film is an N-type semiconductor.

The $(Cd_{1-x}Zn_x)_3As_2/MoO_3$ thin film array heterojunction devices were fabricated and measured to evaluate the photoelectric performance. We carried out systematic study of the performance of the devices from the following aspects: *I–V* performance, the effects of diverse excitation wavelength, power density of laser and bias voltage (V_{bias}) on photocurrent (I_{ph}). Fig. 2a reveals *I–V* curves (V_{bias} from −5 V to 5 V) of the device, which has improved by more than 12 times the distinguished *I–V* rectification characteristics compared with those of other DSM-based devices.[22,24,27] Under the illumination of diverse wavelengths, I_{ph} shows a remarkable photoresponse and wide spectral response from VL to the mid-IR region. A pulse laser with broadband wavelength is used to demonstrate the optoelectronic properties of the device, showing switches between the high (on) and low conductance (off) states. Due to the photovoltaic

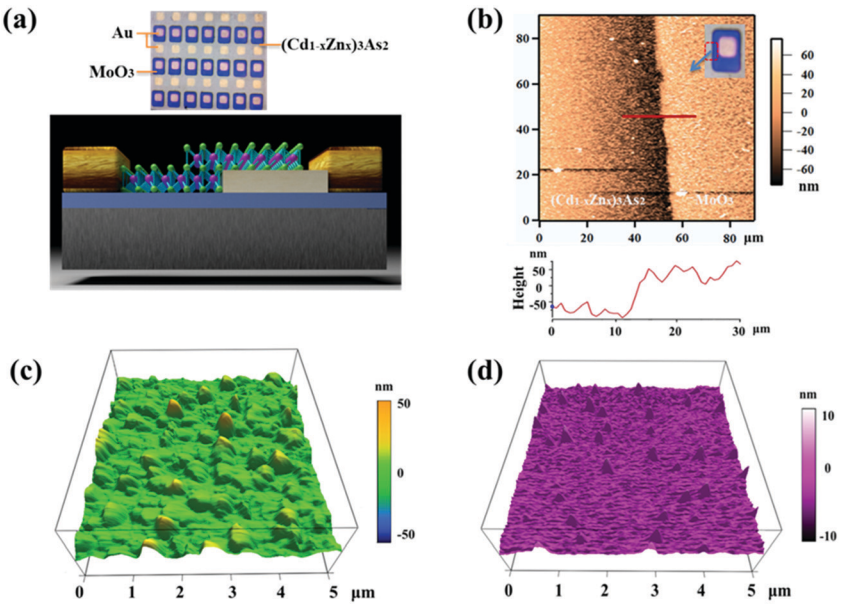

Fig. 1 Structure and morphology of the device. (a) Array device schematic diagram and physical diagram. (b) AFM diagram of the $(Cd_{1-x}Zn_x)_3As_2/MoO_3$ heterojunction. The altitude intercept between $(Cd_{1-x}Zn_x)_3As_2$ and MoO_3 layers is about 100 nm. (c and d) AFM surface diagrams of $(Cd_{1-x}Zn_x)_3As_2$ and MoO_3 thin films. AFM test region is 5 μm × 5 μm.

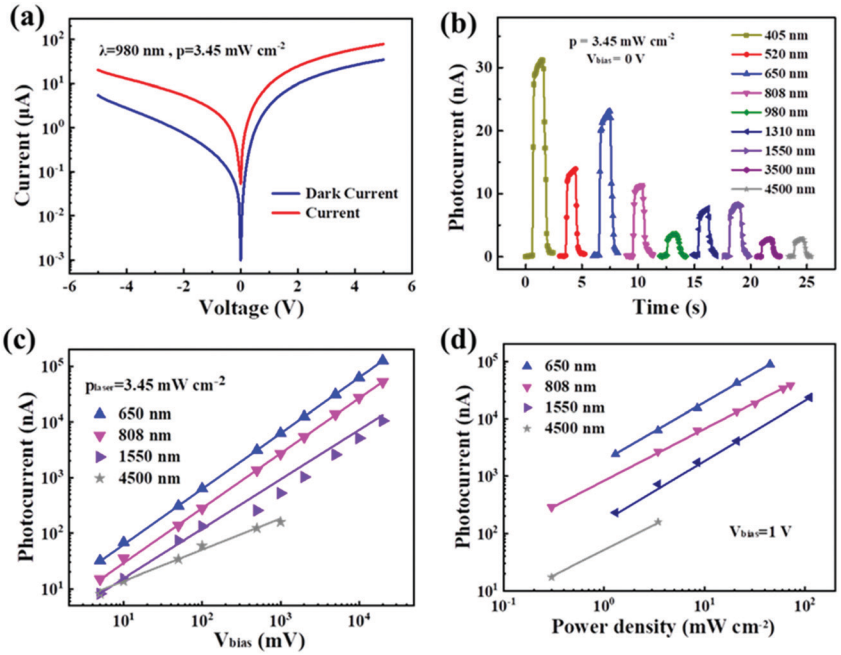

Fig. 2 Optoelectronic properties of the $(Cd_{1-x}Zn_x)_3As_2/MoO_3$ thin film array heterojunction photodetector. (a) The photodetector I–V curves with and without light irradiation @ 980 nm. (b) The I_{ph} curves of the device under different waveband light irradiation under V_{bias} = 0 V with a 3.45 mW cm^{-2} irradiation power intensity. (c) The I_{ph} curves of the device under different V_{bias} with a 3.45 mW cm^{-2} laser power intensity. (d) The I_{ph} curves of the device under different laser power densities, while V_{bias} = 1 V.

effect, the device can operate without power supply, and I_{ph} at the VL region is larger than the IR ones (Fig. 2b).

For detailed photodetection ability, I_{ph} is linearly dependent on both V_{bias} (Fig. 2c and Fig. S4a, ESI†) and laser power density (Fig. 2d and Fig. S4b, ESI†). With V_{bias} increasing from 0 to 20 V, I_{ph} (@650 nm) increases from 12 nA to 126 μA with a 3.45 mW cm^{-2} irradiation power density. When the irradiation power changes from 1.3 mW cm^{-2} to 45 mW cm^{-2}, I_{ph} (@650 nm) linearly rises by 35 times under V_{bias} = 1 V. So the device has a stable linear light detection capability when the external conditions change.

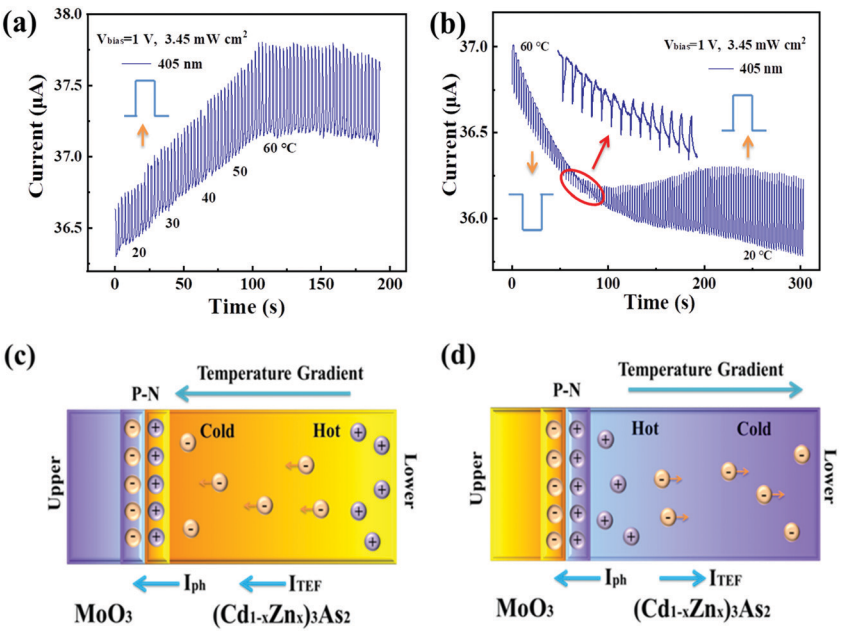

Fig. 3 Current variation characterization of the $(Cd_{1-x}Zn_x)_3As_2/MoO_3$ (100 nm/100 nm) thin film heterojunction device. (a and b) The heating and cooling processes of the device, respectively. The inset curve is a partial magnification of the reversal current position. (c and d) The schematic diagrams of carrier distribution corresponding to heterojunction contact interfaces under heating and cooling conditions, respectively.

We investigate the post-growth annealing method to better optimize the photoelectric properties of the device by enhancing the intermolecular interaction of thin films.[23,27,29] The post-growth annealing temperature is set to be less than 140 °C to avoid $(Cd_{1-x}Zn_x)_3As_2$ degradation at the standard atmosphere. Under annealing the temperatures rise, the I_{ph} of the device at different wavebands first increases, then decreases and reaches a maximum value at ~100 °C (Fig. S5a and b, ESI†). With the increase of annealing temperature, the $(Cd_{1-x}Zn_x)_3As_2$ thin film surface RMS variation trend is consistent with I_{ph}, indicating the effectiveness of annealing treatment (Fig. S6, ESI†).

Photoelectric devices usually exhibit merely single type (positive or negative) I_{ph} under light irradiation, regardless of the doping degree of an external electric field or physical/chemical modification modulation. Intriguingly, in the $(Cd_{1-x}Zn_x)_3As_2/MoO_3$ (100 nm/100 nm) thin film heterojunction device, the current reversal phenomenon from negative to positive is observed with changing temperature. In our experiment, the rise and decrease of temperature are achieved by substrate heating and natural cooling on a metal platform. With the temperature rising from 20 °C to 60 °C, the I_{dark} and I_{ph} of the device grow gradually and reach saturation at 60 °C (Fig. 3a). With the temperature decreasing from 60 °C to 20 °C, I_{dark} decreases gradually, while I_{ph} decreases gradually and changes from negative to positive (Fig. 3b). In addition, the current reversal phenomenon is also detected in the $(Cd_{1-x}Zn_x)_3As_2/MoO_3$ (50 nm/100 nm) heterojunction devices (Fig. S7, ESI†).

Through systematical analysis, we discover that the negative I_{ph} is derived from thermoelectromotive force (TEF), as clarified by the schematic diagram in Fig. 3c. Due to the semimetal characteristics, the $(Cd_{1-x}Zn_x)_3As_2$ thermal velocity characteristic is stronger than heat-resistant MoO_3. Therefore, TEF is mainly determined by the $(Cd_{1-x}Zn_x)_3As_2$ layer. When the device is heated, the temperature drops from the $(Cd_{1-x}Zn_x)_3As_2$ bottom surface to the top MoO_3 surface. The high temperature results in high background carrier concentration, which leads I_{dark} to rise. I_{dark} in Fig. 3a increases gradually with the increase of temperature and finally saturates. When the temperature rises, TEF outputs a positive voltage, and I_{TEF} and I_{ph} are in the same direction (Fig. 3c), which have a superposition effect. Thus, the output current gradually increases in Fig. 3a. In contrast, when the temperature drops, the temperature gradient direction is from the upper surface of $(Cd_{1-x}Zn_x)_3As_2$ to the lower surface (Fig. 3d). The electron diffuses from the hot end to the cold, causing $(Cd_{1-x}Zn_x)_3As_2$ to form a positive and negative space charge in the hot end and the cold, respectively. TEF outputs a negative voltage, with the direction opposite to I_{ph}. I_{TEF} and I_{ph} produce a competitive effect. So under the double action of light illumination and temperature variation element, the current reversal phenomenon in Fig. 3b appears.

We present the contact interface energy band diagram of the $(Cd_{1-x}Zn_x)_3As_2/MoO_3$ heterojunction (Fig. 4a) to reveal the broadband response mechanism. According to different band-gap characteristics of the two materials, when pump photon energy is higher than the MoO_3 band-gap, *e.g.* 450 nm, both MoO_3 and $(Cd_{1-x}Zn_x)_3As_2$ play a dominant role. In this state, both materials can produce photon-generated carriers, which can be separated rapidly through the action of the junction area. When the illumination photon energy exceeds MoO_3 below $(Cd_{1-x}Zn_x)_3As_2$, *e.g.* 3500 nm, MoO_3 possesses no absorption capacity.[26,30–34] At this point, only $(Cd_{1-x}Zn_x)_3As_2$ absorbs light and generates the photoelectron hole pairs, while MoO_3 serves as the carrier transport channel.

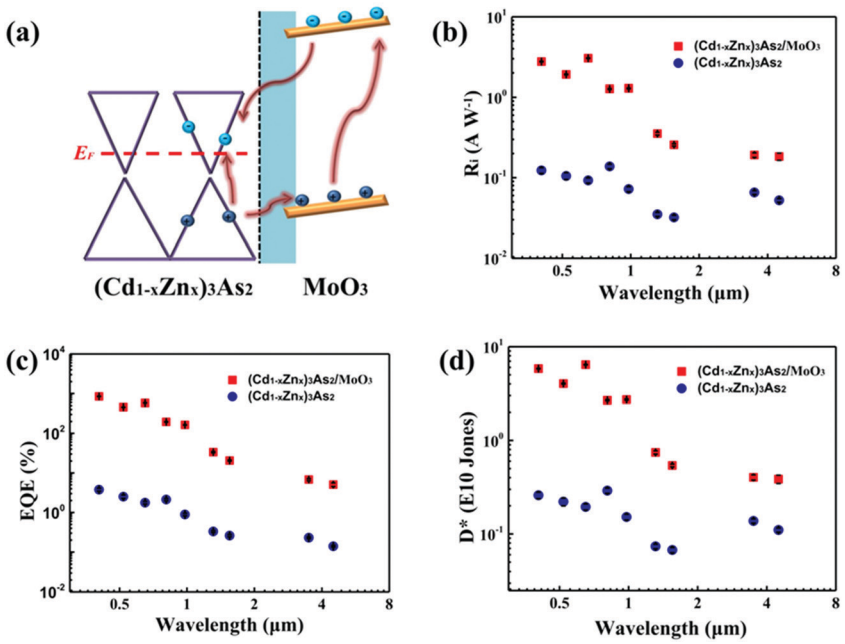

Fig. 4 Optoelectronic performance of the device. (a) The contact energy band diagram of the $(Cd_{1-x}Zn_x)_3As_2/MoO_3$ heterojunction. The E_f of $(Cd_{1-x}Zn_x)_3As_2$ and MoO_3 are nearly −4.3 eV and −5.3 eV, respectively. (b, c) and d) The R_i, D^* and EQE curves of the $(Cd_{1-x}Zn_x)_3As_2/MoO_3$ thin film heterojunction array device under different wavelength laser irradiation, respectively.

To get a deeper insight into the properties of the device, R_i, EQE and D^* are researched at different wavebands, where R, EQE and D^* represent the levels of the photoelectric device to produce I_{ph} under light intensity, the efficiency of absorbing and converting incident light and the ability to detect the minimum illumination signal, respectively.[34–37] Formulas are given as follows:

$$I_{ph} = I_{light} - I_{dark} \quad (1)$$

$$R_i = \frac{I_{ph}}{p} \quad (2)$$

$$EQE = \frac{I_{ph}}{e\phi} = R_i\frac{h\nu}{e} \quad (3)$$

$$D^* = \frac{R_i\sqrt{S}}{\sqrt{2qI_{dark}}} \quad (4)$$

where p, e, ϕ, $h\nu$, S and I_{dark} represent illumination power density, electron charge, photon flux, photon energy, channel effective area and dark current, respectively.[37–39]

The calculated R_i, EQE, and D^* are shown in Fig. 4b–d. The maximum R_i of the heterojunction device can achieve 3.1 A W^{-1} (@650 nm), with crest values D^* and EQE reaching 6.4 $\times$ 10^{10} Jones and 855.8%, respectively. Furthermore, in the mid-IR region (4500 nm), R_i, D^* and EQE can reach as high as 0.2 A W^{-1}, 0.4 $\times$ 10^{10} Jones and 5.6%, respectively. The above-mentioned performance of the heterojunction device is nearly 100 times higher than that of the $(Cd_{1-x}Zn_x)_3As_2$ one and previously reported DSM-based ones.[25,29,36–38]

The interface contact between MoO_3 and $(Cd_{1-x}Zn_x)_3As_2$ is similar to a Schottky junction, and $(Cd_{1-x}Zn_x)_3As_2$ can be considered as a good conductor because of the TSS effect. According to the Fermi level (E_f) of MoO_3 and DSMs are different, the energy band bending at the interface is caused by the hole-trap-assisted electron tunneling effect.[32,34] Due to the lower E_f of DSMs the electrons flow from MoO_3 to DSMs. The built-in electric field is formed to impede the electron diffusion. MoO_3 owns a large number of electron traps and captures photo-generated electrons, which travel to the junction region under the action of the electric field. As a result, the junction is narrowed with higher electric field intensity, causing the electron tunneling in great quantities from DSMs into MoO_3, known as the multiplier tunneling effect. The key figure of merit, EQE, reaches more than 100% due to the aforementioned effects.[39–42] With high V_{bias} (5–20 V), high electric field intensity in the P–N junction region makes the junction region similar to avalanche diode discharge, where the photo-generated hole–electron pairs possess high move speed. Due to their drastic kinetic energy, a collision ionization phenomenon occurs in the process of motion, and several or dozens of secondary new electron–hole pairs can be generated. Furthermore, these can produce three or four hole–electron pairs. Through this, electron–hole pairs are generated dozens of times, creating a greater current. Hence, this is another reason for the device to achieve an EQE of more than 100%.

In addition, we studied the influence of different thickness $(Cd_{1-x}Zn_x)_3As_2$ and MoO_3 thin film layers on the R_i performance of the photoelectric devices (Fig. S8, ESI†). The response times (τ_{on} and τ_{off}) of the $(Cd_{1-x}Zn_x)_3As_2/MoO_3$ heterojunction thin film photodetector are 30 ms and 280 ms @ 808 nm (Fig. S9, ESI†), respectively. The noise diagrams of pure $(Cd_{1-x}Zn_x)_3As_2$ and $(Cd_{1-x}Zn_x)_3As_2/MoO_3$ thin film heterojunction are displayed (Fig. S10, ESI†). The heterojunction can reduce the noise by nearly two orders of magnitude than the pure one, leading to the higher optoelectronic performance.[40–43] In addition, both R_i and D^* of the device increase as the power density decreases (Fig. S11, ESI†), which is due to the contact interface photo-gating effect.

We especially list and compare the performance of relevant DSM-based and other types of material (topological insulators, graphene, and TMDs)-heterojunction devices (Table 1) with that of the $(Cd_{1-x}Zn_x)_3As_2/MoO_3$ heterojunction device for a more comprehensive comparison. The devices prepared in this experiment have significant improvement in R_i, EQE and D^* compared with other DSM-based devices, but there is still a great space for improvement compared with other state-of-the art materials and their performance. In addition, the device also possesses better time stability than the Cd_3As_2/organics (pentacene) device under standard atmosphere and room temperature conditions (Fig. 5a). Compared with the organic semiconductors, MoO_3 can better maintain the stability peculiarity of DSM thin films.[18] And the performance of the $(Cd_{1-x}Zn_x)_3As_2/MoO_3$ thin film heterojunction remains unchanged at more than 30 days without any protective measures.

Table 1 Photoelectric performance comparison of the device of this work with other previously reported photoelectric devices

Active materials	R_i (mA W^{-1})	Wavelength range (nm)	EQE (%)	D^* (Jones)	Ref.
Cd_3As_2 crystal nanowire/plate	5.9	532–10 600	—	—	20
Cd_3As_2 crystal platelets	0.3	1064	—	—	21
Bi_2Se_3/MoO_3 thin film	1.6 $\times$ 10^7	405–1550	4.9 $\times$ 10^4	5.8 $\times$ 10^{11}	24
Bi_2Te_3/pentacene thin film	14.9 $\times$ 10^3	450–3500	2840	—	33
Pure Cd_3As_2 thin film	12.5	450–10 600	2.5	6.5 $\times$ 10^7	42
Cd_3As_2/pentacene thin film	36.2	450–10 600	7.3	1.9 $\times$ 10^7	42
Cd_3As_2/DPEPO thin film	729	365–10 600	112	7.9 $\times$ 10^9	46
Cd_3As_2/PEDOT:PSS thin film	104	405–10 600	21.2	1.1 $\times$ 10^9	46
$MoTe_2$/graphene nanosheet	200	1265–1330	—	—	47
WSe_2/Bi_2Te_3 thin film	20.5 $\times$ 10^3	375–1550	—	—	48
$(Cd_{1x}Zn_x)_3As_2$ thin film	147	405–4500	4.1	2.9 $\times$ 10^9	This work
$(Cd_{1x}Zn_x)_3As_2/MoO_3$ thin film	3.1 $\times$ 10^3	405–4500	855.8	6.42 $\times$ 10^{10}	This work

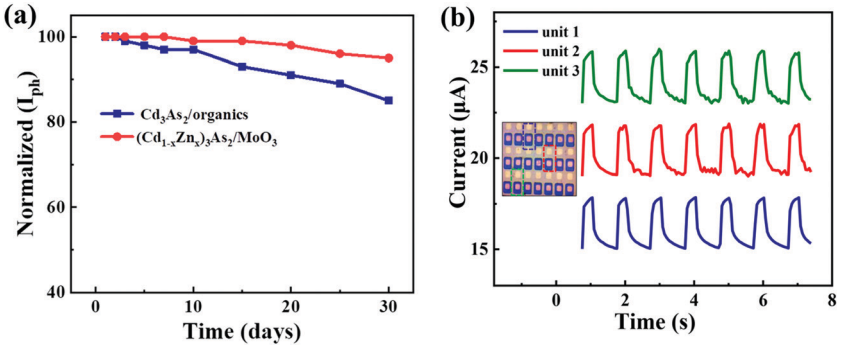

Fig. 5 The comparison diagram of air stability and unit performance of the $(Cd_{1-x}Zn_x)_3As_2/MoO_3$ array devices. (a) The curves of $(Cd_{1-x}Zn_x)_3As_2/MoO_3$ and Cd_3As_2/organics (pentacene) thin film heterojunction device I_{ph} effects by different times under atmospheric conditions at room temperature. The I_{ph} values in the diagram are normalized. (b) Three different unit I_{ph} diagrams of the same device @ 808 nm. The power intensity was 3.45 mW cm^{-2}. Inset is the physical diagram of array device, and in dotted boxes are the selected test units.

The unit stability of an array device is a prerequisite to determine whether array devices can finally be widely used.[25,35,44–50] To this end, we randomly tested three different units in the same array device and found that the I_{ph} properties of these units were indiscriminate (Fig. 5b). This proves that the array device prepared by this method possesses great application potential in the field of photoelectric detection in the future.[51–54]

For completeness, the absorption characteristics were tested in detail to comprehensively characterize the I_{ph} generation mechanism of the $(Cd_{1-x}Zn_x)_3As_2/MoO_3$ thin film heterojunction device. Compared with pure $(Cd_{1-x}Zn_x)_3As_2$ (Fig. S12, ESI†), the $(Cd_{1-x}Zn_x)_3As_2/MoO_3$ can improve absorption from 200 nm to 4600 nm (UV-mid-IR). This is also another reason for the higher R_i of the $(Cd_{1-x}Zn_x)_3As_2/MoO_3$ device than that of the pure one (Fig. 4b).

3. Conclusions

In conclusion, our results have a profound impact on the understanding and development of practical DSM photoelectric devices. The 3D $(Cd_{1-x}Zn_x)_3As_2/MoO_3$ thin film heterojunction array photodetectors have been successfully prepared. The device exhibits a current reversal phenomenon under the action of both light illumination and temperature variation elements. The working mechanism of this phenomenon is systematically analyzed and interpreted. In particular, the array device units possess repeatability and excellent time stability of the photoelectric performance. With record-high directly measured photoelectric properties, our results extend the potential of DSMs for practical use in the fields of array applications. Hence, the 3D DSMs/MoO_3 thin film heterojunction array device possesses distinguished photoelectric performance and will offer a whole novel method to apply 3D DSMs in the mid-IR detection field.

4. Experimental

4.1 Thin film preparation

$(Cd_{1-x}Zn_x)_3As_2$ and MoO_3 thin films used in the experiments were prepared by the method of MBE and thermal deposition.[55–57] The instrument model of molecular beam epitaxy (MBE) system is PERKIN ELMER 425 B. First, a deeply cleaned sapphire substrate was selected and put into the MBE system, and heated at 550 °C for 30 min to remove the gas content in the cavities. After the vacuum degree reached 1.1×10^{-9} Torr, the substrate was heated to 190 °C. Then, the CdTe buffer layer began to grow; the growth temperatures of Cd and Te sources were 155 °C and 295 °C (15 min), respectively. Finally, the substrate temperature was maintained at 120 °C, the temperatures of Zn source and Cd_3As_2 source were 230 °C and 330 °C, respectively, and the growth time was about 40 min. During the MoO_3 thin film deposition process, the deposition rate was 0.05 nm s^{-1} with a vacuum degree of 6×10^{-4} Pa at 600 °C. To make good contact at the DSMs/MoO_3 interface, the temperature needs to still be maintained at 600 °C (30 min) after MoO_3 thin film deposition was completed. The thickness of the electrode was 120 nm, which was prepared by the thermal evaporation method. The channel size of the prepared device was 200 μm × 200 μm.

4.2 Characterization of thin film properties

The AFM surface undulation of $(Cd_{1-x}Zn_x)_3As_2$, MoO_3 and the heterojunction thin films were characterized by an Asylum Research MFP-3D instrument. UV-NIR absorption and mid-IR absorption of the diverse thin films were tested by a Shimadzu UV-2600 instrument and an IS50R FTIR instrument, respectively. The instrument models of XPS test and EDS mapping test were Escalab 250Xi and FEI Inspect-F50, respectively.

4.3 Photoelectric performance characterization

The photoelectric performance (I_{ph}, I–V curves) were test by a Keithley 2636B at room temperature under ordinary pressure. The noise diagrams of the devices were measured by a FS-Pro all-in-one multifunctional semiconductor parameter testing system. A heating table (JF-956s) was used to directly heat the samples in the experiment, and the temperature was measured by a Smart Sensor AR852B instrument. The cooling process involves placing the heated sample directly on a cold metal plate.

Author contributions

J. W. and F. X. designed and conducted this work. M. Y., Q. L., Y. Y., J. H., H. Z. and X. X. conducted the experimental measurements. Z. H., J. G., T. Y., Z. W. and Y. J. provided suggestions and assistance in the experimental work. All the authors discussed the experimental results.

Conflicts of interest

The authors declare no conflict of interest.

Acknowledgements

This work is supported by the National Outstanding Youth Science Fund Project of the National Natural Science Foundation of China (No. 61922022), the Science Fund for Innovative Research Group Project of the National Natural Science Foundation of China (No. 61421002), the National Natural Science Foundation of China (No. 61674079, 61875031, 61674040, 11934005, and 11874116), the Science and Technology Commission of Shanghai (Grant No. 19511120500) and the Sichuan Science and Technology Program (Grant No. 2020JDRC0061, and 2019JDRC0072).

References

1 A. Pospischil, M. Humer, M. Furch, D. Bchmann, R. Guider, T. Fromherz and T. Mueller, *Nat. Photonics*, 2013, **7**, 892–896.
2 J. Shen, R. Zhang, Y. Su, B. Shi, X. You, W. Guo, Y. Ma, J. Yuan, F. Wang and Z. Jiang, *J. Mater. Chem. A*, 2019, **7**, 18063–18071.
3 M. Casalino, U. Sassi, I. Goykhman, A. Eiden, E. Lidorikis, S. Milana, D. Fazio, F. Tomarchio, M. Iodice, G. Coppola and A. Ferrari, *ACS Nano*, 2017, **11**, 10955–10963.
4 I. Romanenko, M. Lechner, F. Wendler, C. Hörenz, C. Streb and F. H. Schacher, *J. Mater. Chem. A*, 2017, **5**, 15789–15796.
5 X. Gan, R. J. Shiue, Y. Gao, I. Meric, T. F. Heinz, K. Shepard, J. Hone, S. Assefa and D. Englund, *Nat. Photonics*, 2013, **7**, 883–887.
6 F. Koppens, T. Mueller, Ph. Avouris, A. Ferrari, M. Vitiello and M. Polini, *Nat. Nanotechnol.*, 2014, **9**, 780–793.
7 K. Kang, T. Li, E. Sohn, J. Shan and K. Mak, *Nat. Photonics*, 2019, **18**, 324–328.
8 J. Han, J. Wang, M. Yang, X. Kong, X. Chen, Z. Huang, H. Guo, J. Gou, S. Tao, Z. Liu, Z. Wu, Y. Jiang and X. Wang, *Adv. Mater.*, 2018, 1804020.
9 N. Youngblood, C. Chen, S. Koester and M. Li, *Nat. Photonics*, 2015, **9**, 247–252.
10 T. Yang, X. Wang, B. Zheng, Z. Qi, C. Ma, Y. Fu, Y. Fu, M. P. Hautzinger, Y. Jiang, Z. Li, P. Fan, F. Li, W. Zheng, Z. Luo, J. Liu, B. Yang, S. Chen, D. Li, L. Zhang, S. Jin and A. Pan, *ACS Nano*, 2019, **13**, 7996–8003.
11 M. Long, Y. Wang, P. Wang, X. Zhou, H. Xia, C. Luo, S. Huang, G. Zhang, H. Yan, Z. Fan, X. Wu, X. Chen, W. Lu and W. Hu, *ACS Nano*, 2019, **13**, 2511–2519.
12 Q. Guo, A. Pospischil, M. Bhuiyan, H. Jiang, H. Tian, D. Farmer, B. Deng, C. Li, S. Han, H. Wang, Q. Xia, T. Ma, T. Mueller and F. Xia, *Nano Lett.*, 2016, **16**, 4648–4655.
13 A. Khanikaev and G. Shvets, *Nat. Photonics*, 2017, **11**, 763–773.
14 L. He, F. Xiu, X. Yu, M. Teague, W. Jiang, Y. Fan, X. Kou, M. Lang, Y. Wang, G. Huang, N. Yeh and K. Wang, *Nano Lett.*, 2012, **12**, 1486–1490.
15 E. Zhang, P. Wang, Z. Li, H. Wang, C. Song, C. Huang, Z. Chen, L. Yang, K. Zhang, S. Lu, W. Wang, S. Liu, H. Fang, X. Zhou, H. Yan, J. Zou, X. Wan, P. Zhou, W. Hu and F. Xiu, *ACS Nano*, 2016, **10**, 8067–8077.
16 C. Wang, Q. He, U. Halim, Y. Liu, E. Zhu, Z. Lin, H. Xiao, X. Duan, Z. Feng, R. Cheng, N. Weiss, G. Ye, Y. C. Huang, H. Wu, H. C. Cheng, I. Shakir, L. Liao, X. Chen, W. A. Goddard III and Y. Huang, *et al.*, *Nature*, 2018, **555**, 231–236.
17 Z. Hu, Q. Li, B. Lei, J. Wu, Q. Zhou, C. Gu, X. Wen, J. Wang, Y. Liu, S. Li, Y. Zheng, J. Lu, J. He, L. Wang, Q. Xiong, J. Wang and W. Chen, *Adv. Mater.*, 2018, **30**, e1801931.
18 Z. Hu, Q. Li, B. Lei, Q. Zhou, D. Xiang, Z. Lyu, F. Hu, J. Wang, Y. Ren, R. Guo, E. Goki, L. Wang, C. Han, J. Wang and W. Chen, *Angew. Chem., Int. Ed.*, 2017, **56**, 9131–9135.
19 C. Zhang, Y. Zhang, X. Yuan, S. Lu, J. Zhang, A. Narayan, Y. Liu, H. Zhang, Z. Ni, R. Liu, E. S. Choi, A. Suslov, S. Sanvito, L. Pi, H. Z. Lu, A. C. Potter and F. Xiu, *Nature*, 2019, **565**, 331–336.
20 Q. Wang, C. Z. Li, S. Ge, J. G. Li, W. Lu, J. Lai, X. Liu, J. Ma, D. P. Yu, Z. M. Liao and D. Sun, *Nano Lett.*, 2017, **17**, 834–841.
21 N. Yavarishad, T. Hosseini, E. Kheirandish, C. P. Weber and N. Kouklin, *Appl. Phys. Express*, 2017, **10**, 052201.
22 X. Chen, X. Liu, B. Wu, H. Nan, H. Guo, Z. Ni, F. Wang, X. Wang, Y. Shi and X. Wang, *Nano Lett.*, 2017, **17**, 6391–6396.
23 Y. Sun, Y. Meng, R. Dai, Y. Yang, Y. Xu, S. Zhu, Y. Shi, F. Xiu and F. Wang, *Opt. Lett.*, 2019, **44**, 4103–4106.
24 M. Yang, Q. Han, X. Liu, J. Han, Y. Zhao, L. He, J. Gou, Z. Wu, X. Wang and J. Wang, *Adv. Funct. Mater.*, 2020, 1909659.
25 L. Zdanowicz and W. Zdanowicz, *Phys. Status Solidi*, 1964, **6**, 227–234.
26 H. Lu, X. Zhang, Y. Bian and S. Jia, *Sci. Rep.*, 2017, **7**, 3148.
27 S. Nishihaya, M. Uchida, Y. Nakazawa, M. Kriener, Y. Kozuka, Y. Taguchi and M. Kawasaki, *Sci. Adv.*, 2018, **4**, eaar5668.
28 J. Wang, J. Han, X. Chen and X. Wang, *InfoMat*, 2019, **1**, 33–53.
29 G. Konstantatos and E. Sargent, *Nat. Nanotechnol.*, 2010, **5**, 391–400.
30 P. Hu, L. Wang, M. Yoon, J. Zhang, W. Feng, X. Wang, Z. Wen, J. C. Idrobo, Y. Miyamoto, D. B. Geohegan and K. Xiao, *Nano Lett.*, 2013, **13**, 1649–1654.
31 P. J. Jadhav, A. Mohanty, J. Sussman, J. Lee and M. A. Baldo, *Nano Lett.*, 2011, **11**, 1495–1498.
32 B. Ehrler, B. J. Walker, M. L. Bohm, M. W. Wilson, Y. Vaynzof, R. H. Friend and N. C. Greenham, *Nat. Commun.*, 2012, **3**, 1019.

33 M. Yang, J. Wang, Y. Zhao, L. He, C. Ji, X. Liu, H. Zhou, Z. Wu, X. Wang and Y. Jiang, *ACS Nano*, 2019, **13**, 755–763.
34 H. Zhong, K. Xu, Z. Liu, G. Xu, L. Shi, Y. Fan, J. Wang, G. Ren and H. Yang, *J. Appl. Phys.*, 2014, **115**, 013701.
35 Y. Feng, L. Ling, J. Nie, K. Han, X. Chen, Z. Bian, H. Li and Z. L. Wang, *ACS Nano*, 2017, **11**, 12411–12418.
36 K. Zhang, T. Zhang, G. Cheng, T. Li, S. Wang, W. Wei, X. Zhou, W. Yu, Y. Sun, P. Wang, D. Zhang, C. Zeng, X. Wang, W. Hu, H. J. Fan, G. Shen, X. Chen, X. Duan, K. Chang and N. Dai, *ACS Nano*, 2016, **10**, 3852–3858.
37 J. Miao, B. Song, Q. Li, L. Cai, S. Zhang, W. Hu, L. Dong and C. Wang, *ACS Nano*, 2017, **11**, 6048–6056.
38 R. A. John, N. Yantara, Y. F. Ng, G. Narasimman, E. Mosconi, D. Meggiolaro, M. R. Kulkarni, P. K. Gopalakrishnan, C. A. Nguyen, F. De Angelis, S. G. Mhaisalkar, A. Basu and N. Mathews, *Adv. Mater.*, 2018, **30**, e1805454.
39 H. Zhang, C. X. Liu, X. L. Qi, X. Dai, Z. Fang and S. C. Zhang, *Nat. Phys.*, 2009, **5**, 438–442.
40 D. Hsieh, Y. Xia, L. Wray, D. Qian, A. Pal, J. H. Dil, J. Osterwalder, F. Meier, G. Bihlmayer and C. L. Kane, *Science*, 2009, **323**, 919–922.
41 K. Cho, J. Pak, S. Chung and T. Lee, *ACS Nano*, 2019, **13**, 9713–9734.
42 M. Yang, J. Wang, J. Han, J. Ling, C. Ji, K. Xiao, X. Liu, Z. Huang, J. Gou, Z. Liu, F. Xiu and Y. Jiang, *ACS Photonics*, 2018, **5**, 3438–3445.
43 H. Qiao, J. Yuan, Z. Xu, C. Chen, S. Lin, Y. Wang, J. Song, Y. Liu, Q. Khan and Y. H. Hui, *ACS Nano*, 2015, **9**, 1886–1894.
44 X. Zhang, H. Tang, J. Huang, L. Luo, J. Zapien and S. Lee, *Nano Lett.*, 2011, **11**, 4626–4630.
45 J. Yao, Z. Zheng and G. Yang, *J. Mater. Chem. C*, 2016, **4**, 7831–7840.
46 M. Yang, J. Wang, Y. Yang, Q. Zhang, C. Ji, G. Wu, Y. Su, J. Gou, Z. Wu, K. Yuan, F. Xiu and Y. Jiang, *J. Phys. Chem. Lett.*, 2019, **10**, 3914–3921.
47 N. Flöry, P. Ma, Y. Salamin, A. Emboras, T. Taniguchi, K. Watanabe, J. Leuthold and L. Novotny, *Nat. Nanotechnol.*, 2020, **15**, 118–124.
48 H. Liu, X. Zhu, X. Sun, C. Zhu, W. Huang, X. Zhang, B. Zheng, Z. Zou, Z. Luo, X. Wang, D. Li and A. Pan, *ACS Nano*, 2019, **13**, 13573–13580.
49 L. Britnell, R. Ribeiro, A. Eckmann, R. Jalil, B. Belle, A. Mishchenko, Y. Kim, R. Gorbachev, T. Georgiou, S. Morozov, A. Grigorenko, A. Geim, C. Casiraghi, A. Castro Neto and K. Novoselov, *Science*, 2013, **340**, 1311–1314.
50 Y. Liu, J. Guo, E. Zhu, L. Liao, S. J. Lee, M. Ding, I. Shakir, V. Gambin, Y. Huang and X. Duan, *Nature*, 2018, **557**, 696–700.
51 M. Yang, J. Wang, Y. Zhao, L. He, C. Ji, H. Zhou, J. Gou, W. Li, Z. Wu and X. Wang, *ACS Nano*, 2019, **13**, 10810–10817.
52 F. Wang, L. Li, W. Huang, L. Li, B. Jin, H. Li and T. Zhai, *Adv. Funct. Mater.*, 2018, **28**, 1802707.
53 A. Sharma, A. Srivastava, T. Senguttuvan and S. Husale, *Sci. Rep.*, 2017, **7**, 17911.
54 T. Zhai, X. Fang, M. Liao, X. Xu, L. Li, B. Liu, Y. Koide, Y. Ma, J. Yao, Y. Bando and D. Golberg, *ACS Nano*, 2010, **4**, 1596–1602.
55 C. Zhu, F. Wang, Y. Meng, X. Yuan, F. Xiu and H. Luo, *Nat. Commun.*, 2017, **8**, 14111.
56 X. Yu, L. He, M. Lang, W. Jiang, F. Xiu, Z. Liao, Y. Wang, X. Kou, P. Zhang and J. Tang, *Nanotechnology*, 2013, **24**, 015705.
57 M. Hossain, S. Rumyantsev, K. Shahil, D. Teweldebrhan, M. Shur and A. Balandin, *ACS Nano*, 2011, **5**, 2657–2663.